aerospace

MDPI

Article

Combustion Characteristics of a Swirl-Radial-Injection Composite Fuel Grain with Applications in Hybrid Rockets

Ruoyan Wang [1,2], Xin Lin [1,*], Zezhong Wang [1,*], Kun Wu [1], Zelin Zhang [1], Jiaxiao Luo [1,2], Fei Li [1] and Xilong Yu [1,2]

[1] State Key Laboratory of High Temperature Gas Dynamics, Chinese Academy of Sciences, Beijing 100190, China; wangruoyan@imech.ac.cn (R.W.)
[2] School of Engineering Science, University of Chinese Academy of Sciences, Beijing 100049, China
* Correspondence: linxin_bit@imech.ac.cn (X.L.); wangzezhong@imech.ac.cn (Z.W.)

Abstract: The combustion characteristics of a swirl-radial-injection composite fuel grain were experimentally and numerically investigated. This composite grain permits swirl-radial oxidizer injection based on three hollow helical blades, each having a constant hollow space allowing uniform oxidizer injection into the main chamber along the axial direction. The oxidizer enters from channel inlets located along a hollow outer wall. This wall, together with the three blades, is fabricated as one piece from acrylonitrile-butadiene-styrene using three-dimensional printing. Paraffin-based fuel is embedded in the spaces between adjacent blades. Firing tests were conducted with gaseous oxygen as the oxidizer, using oxidizer mass flow rates ranging from 7.45 to 30.68 g/s. Paraffin-based fuel grains using conventional fore-end injection were used for comparison. Regression rate boundaries were determined taking into account the erosion of the oxidizer channels. The data show that the regression rate was significantly increased even at the lower limit. Images of the combustion chamber flame and of the exhaust plume were also acquired. The flame was found to be concentrated in the main chamber and a smoky plume was observed, consistent with the high regression rate. A three-dimensional simulation was employed. The present design was found to improve fuel/oxidizer mixing and combustion efficiency compared with a fuel grain using fore-end injection. Both the experimental results and numerical simulations confirmed the potential of this swirl-radial-injection fuel grain.

Keywords: hybrid rocket engine; swirl-radial injection; regression rate; flame images; combustion efficiency

Citation: Wang, R.; Lin, X.; Wang, Z.; Wu, K.; Zhang, Z.; Luo, J.; Li, F.; Yu, X. Combustion Characteristics of a Swirl-Radial-Injection Composite Fuel Grain with Applications in Hybrid Rockets. *Aerospace* **2023**, *10*, 759. https://doi.org/10.3390/aerospace10090759

Academic Editor: Hui Tian

Received: 30 July 2023
Revised: 23 August 2023
Accepted: 25 August 2023
Published: 28 August 2023

1. Introduction

Hybrid rocket engines (HREs) typically use propulsion systems based on solid fuels combined with liquid oxidizers and have a wide range of potential applications [1]. Compared with solid rocket engines, HREs provide the advantages of adjustable thrust, high safety margins and repeatable start/stop operation. In addition, HREs have simpler structures than liquid rocket engines [2–5]. However, the development of HREs is currently confined by the low fuel grain regression rates associated with these engines [6–9] along with the uneven distribution of regression along the fuel grain. These issues occur because the combustion process in an HRE is primarily driven by boundary-layer fluid dynamics [10–12]. Specifically, the radial airflow generated by the combustion of the fuel surface promotes the development of a boundary layer. This, in turn, produces a flame zone that penetrates through from the surface of the fuel. As a result of these phenomena, convective heat transfer and the rate of enthalpy exchange are significantly reduced [13]. In addition, at axial positions approaching the nozzle, the combustion zone is further removed from the combustion surface, representing the so-called blowing effect [14]. This effect can cause non-uniform fuel regression in the axial direction [15,16]. As a result of this non-uniform regression, the fuel utilization rate is decreased, while both controlling the combustion of the engine and ensuring thermal protection become challenging [17,18].

The regression rate in an HRE can be improved by distorting the boundary layer to increase shear forces in addition to improving the mixing of oxidizer and fuel while promoting heat transfer to the solid fuel [19]. This distortion is typically achieved by optimizing the oxidizer injection process and the fuel grain structure, based on the use of swirling-oxidizer injection techniques and complex port morphologies [20–25]. Bala et al. [20] conducted a series of firing tests using HREs having different length/diameter ratios in conjunction with swirling oxidizer injection at multiple locations. This prior work demonstrated that the regression rate of an HRE having a length/diameter ratio of 24 with multi-location injection was twice that obtained from classical HRE designs. Yuasa et al. [21] investigated a swirling oxidizer engine while applying oxidizer flux values of less than 130 kg/(s·m^2). The regression rate in this engine was 2.7 times higher than that of an engine without swirling-oxidizer injection and the swirl intensity was found to greatly affect the regression rate. However, a strong scouring effect on the fuel grain near the injector was shown to result in uneven regression.

A fuel grain having a complex geometry is another attractive approach to distorting the boundary layer. Riccardo [22] proposed an armored fuel grain comprising both 3D-printed polymeric and paraffin-based fuels. The embedded structure in this grain enhanced the regression rate of the paraffin-based fuel as a result of the irregular burning surface generated during the combustion process. Wang et al. [23] devised a fuel grain having a nested helical structure as a means of improving the regression rate. This grain design mitigated a common difficulty in which the characteristic structure of the propellant disappears as the grain undergoes combustion. Lin et al. [24] and Zhang et al. [25] further enhanced the combustion characteristics of an HRE by employing a metal substrate in conjunction with swirl injection. Although the above methods can effectively increase the regression rate, non-uniform regression along the fuel grain axis still tends to occur.

Oxidizer injection that is uniform in the axial direction can assist in achieving homogeneous regression. This concept was previously used by Shohei et al. to develop the concept of multi-section swirl injection [26,27]. This technique involved simultaneous oxidizer injection at different coaxial positions along the fuel grain such that the oxidizer was distributed more evenly along the axis compared with a traditional fore-end injection system. Even so, the regression rate distribution along the axis of the fuel grain was extremely uneven and erosion was observed near the injection site [28]. Kahraman et al. [29] reported the construction of a distributed tube injector (DTI) installed along the center axis of the combustion chamber to provide radial injection of the oxidizer. This DTI unit provided more uniform injection of oxidizer along the axial direction and resulted in a considerable increase in the regression rate. A drawback to this concept is that the DTI unit is exposed to extremely hot temperatures because of its location at the center of the combustion chamber and so must display exceptional heat resistance.

In the present work, a swirl-radial-injection composite fuel grain for use in HREs is demonstrated. This grain provides both swirling and radial oxidizer injection based on the presence of three spiral, hollow, swirl-radial-injector blades. The design includes a constant hollow gap between blades along the axis direction that allows the oxidizer to be uniformly injected into the main chamber. These blades are made of acrylonitrile-butadiene-styrene (ABS) and fabricated using a three-dimensional printing method. These units served as both a low regression rate fuel and as a support structure for the fuel grain. The gaps between the blades are filled with paraffin-based fuel (high regression rate) to form the overall composite fuel grain. The combustion characteristics of these swirl-radial-injection composite fuel grains were experimentally explored in lab-scale HREs, using gaseous oxygen as the oxidizer. Trials were also performed using paraffin-based fuel grains in conjunction with traditional fore-end injection for comparison. The mass flow rates of the oxidizer in trials with these HREs were in the range of 7.45 to 30.68 g/s. The upper and lower limits of the regression rate were calculated based on mass loss taking into account erosion of the ABS substrate. Visual analysis of the flame both in the combustion chamber and the exhaust plume was employed to monitor the actual combustion process.

In addition, computer simulations were used to evaluate combustion efficiency and flame distribution and to elucidate the mechanism by which the regression rate was increased.

2. Experimental

2.1. Design and Manufacture of a Swirl-Radial-Injection Fuel Grain

As shown in Figure 1, the swirl-radial-injection fuel grain was designed as a composite structure composed of an ABS substrate filled with a paraffin-based fuel. The ABS substrate had a hollow outer wall and three spiral blades that were integrated structures. This fuel grain induced uniform radial oxidizer injection based on the hollow swirl-radial-injector blades inserted at constant intervals. These blades rotated clockwise along the axial direction to induce a swirling flow of the oxidizer while the ABS acted as a low regression rate fuel and provided mechanical support for the fuel grain. The gaps between the blades were filled with a paraffin-based fuel. As shown in Figure 1a, during the operation of the engine, the oxidizer entered a channel located in the cross section of the hollow outer wall and flowed through the hollow blades, after which it was injected into the combustion chamber.

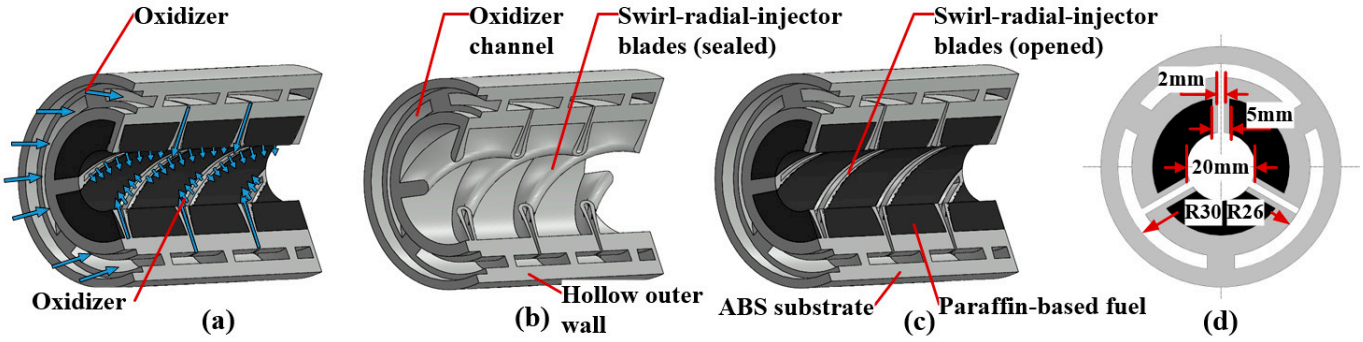

Figure 1. Diagrams of the swirl-radial-injection fuel grain indicating (**a**) the oxidizer flow path, (**b**) the ABS substrate before embedding the paraffin-based fuel, (**c**) the completed grain and (**d**) a cross-sectional view of the grain showing some primary dimensions.

The manufacturing of the swirl-radial-injection fuel grain involved three steps. First, an ABS substrate was prepared using a three-dimensional (3D) printer (Raiser 3D, Pro2 Plus). The outer and interior diameters of the ABS substrate were 70 mm and 16 mm, respectively, while the length was 100 mm. As shown in Figure 1b, the blade outlets were sealed during this step. A centrifugal casting process was subsequently used to inject molten paraffin-based fuel (heated to 120 °C) into the gaps between adjacent blades. During this step, the grain was rotated at 1000 rpm so that the centrifugal force was sufficient to avoid shrinkage and cracking. The paraffin-based fuel comprised 58 wt% paraffin together with 20 wt% polyethylene wax (PE), 10 wt% octadecanoic acid, 10 wt% ethylene vinyl acetate and 2 wt% carbon black. This formulation was employed to ensure that the fuel had suitable mechanical properties [30]. After the grain was filled with paraffin, the port was expanded to a diameter of 20 mm using a turning process. Finally, the outlets of the blades were opened as shown in Figure 1c. Figure 1d provides a cross-sectional view of the fuel grain showing some primary dimensions.

2.2. Lab-Scale Hybrid Rocket Engines

The experimental trials were performed using a lab-scale HRE with gaseous oxygen as the oxidizer. Figure 2 provides a diagram of the test setup, in which an oxygen/methane torch was employed to ignite the fuel grain. The gas supply system, pressure measurement system and nozzle dimensions in the present case were the same as those employed in our previous work [25]. The oxidizer entered the main chamber through an oxidizer supply ring that was connected to the fuel grain through a transition fitting and the mass flow rate of the oxidizer was varied between 7.45 and 30.68 g/s. The combustion chamber was

purged with nitrogen after every firing test. A high-speed camera (iX Cameras, i-Speed 220, London, UK) was used to acquire images of the combustion chamber flame with an exposure time of 2 ms and a frame rate of 1 kHz. A 430 nm narrowband filter was employed to reduce the light intensity transmitted through the optical fiber [31]. The field of view of the chamber flame is indicated by the dotted line frame in the lower part of Figure 2. The images taken by the high-speed camera will be processed with pseudo-color, where the assigned colors represent different gray values only. Video of the exhaust plume was recorded using a Nikon SLR camera.

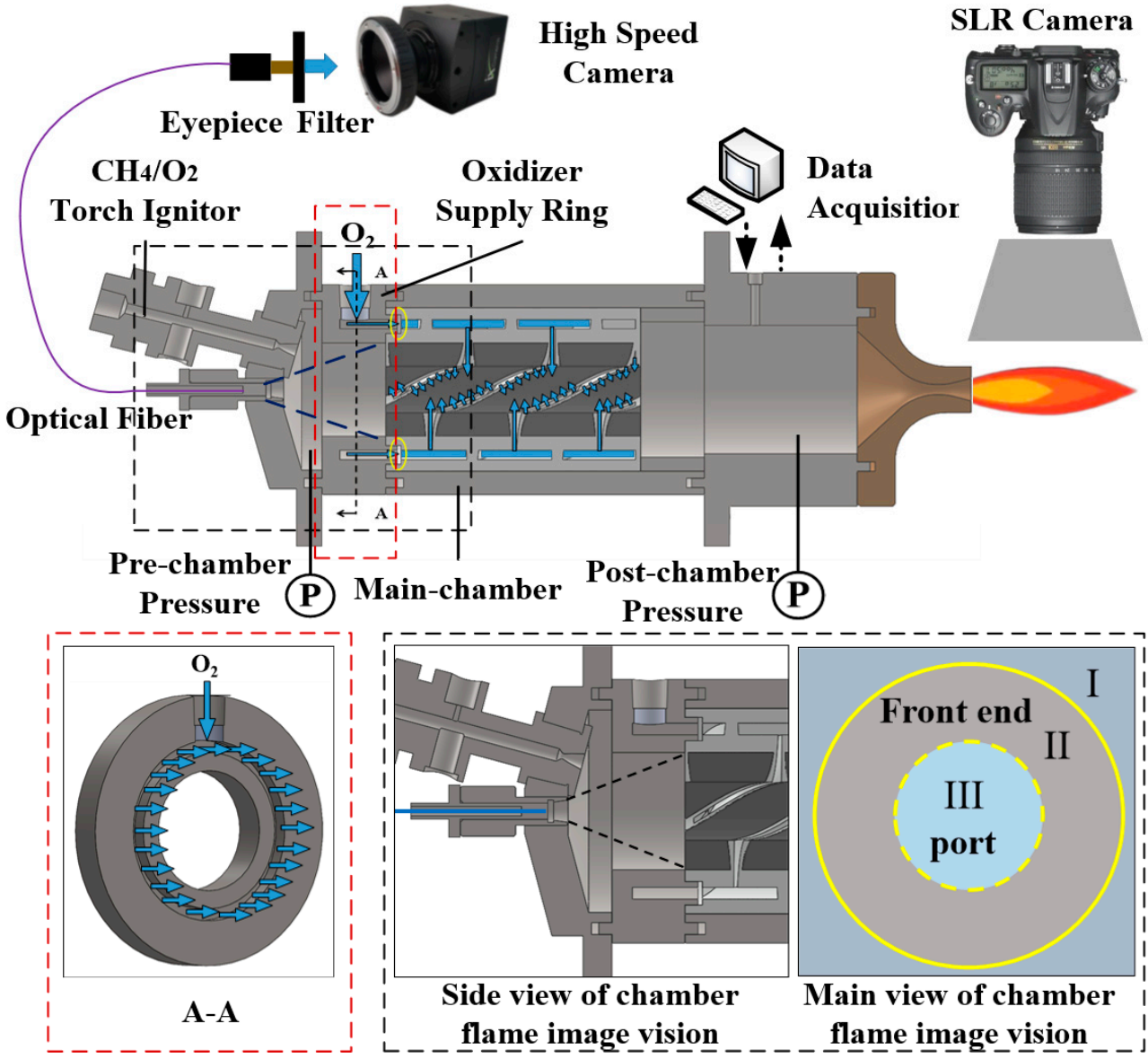

Figure 2. Diagrams of the lab-scale HRE.

2.3. Numerical Simulation Methodology

2.3.1. Computational Domain and Boundary Conditions

The ANSYS Fluent 2022 R2 software (ANSYS 2022 R2; Creator and the location: John Swanson, New York, NY, USA; Software Sourced: Livermore Software Technology Company, Canonburg, PA, USA) program was used to perform combustion simulations. The computational domains for both engine types are presented in Figures 3a and 4a. All walls in the fluid domain were defined as adiabatic. The 3D Navier-Stokes formula was

employed to perform flow simulations and the turbulent flow field was simulated using the SST k-ω turbulent model. The energy equation and species transport equation were coupled. The eddy-dissipation concept model was employed to simulate the combustion process. This model is commonly used to account for interactions between the flame chemistry dynamics and turbulence. The oxidizer and fuel inlets were both defined as mass flow inlets while the outlet was a pressure outlet. Ethylene (C_2H_4) was employed as a surrogate for the present paraffin-based fuel because paraffin is a mixture of saturated alkanes and undergoes combustion in a manner similar to that of ethylene [32]. A 10-step global C_2H_4 reaction mechanism was applied in these simulations [33]. The species associated with the oxygen inlet, fuel inlet and outlet in all cases were set to O_2, C_2H_4 and air, respectively, with temperatures of 300, 1000 and 300 K, respectively. The mass flow rates and pressures for the two cases are summarized in Table 1. In this manner, the combustion flow field, temperature and species distribution were all simulated. Although the present numerical simulation is based on a simplified model, it accurately reflects the combustion characteristics of the two different fuel grains and allows for the additional optimization of the engine structure.

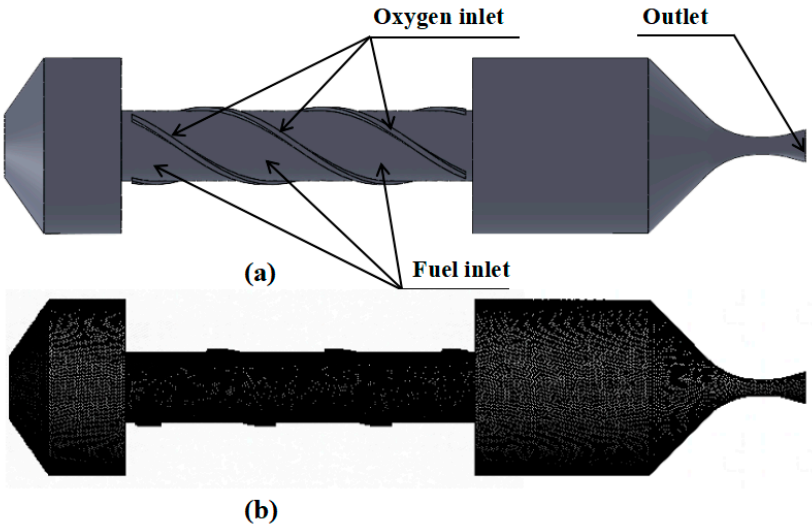

Figure 3. (**a**) The computational domain used to model the swirl-radial-injection engine and (**b**) the same computational domain after applying a mesh.

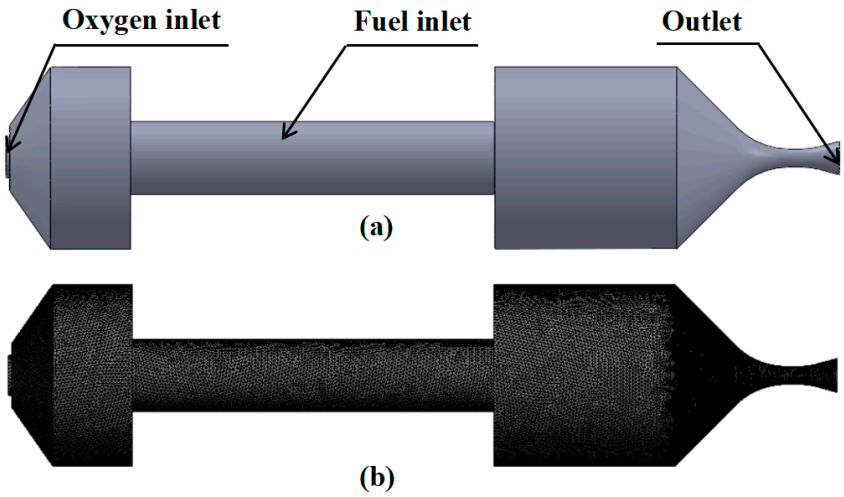

Figure 4. The computational domain for the fore-end injection engine (**a**) before and (**b**) after meshing.

Table 1. Mass flow rates and pressure boundary conditions for the two cases modeled in the present work.

Fuel Grain Configuration	Case No.	Oxygen Inlet, g/s	Fuel Inlet, g/s	Outlet, atm
Fuel grain using fore-end injection	Case 1	18.45	6.72	1
Swirl-radial-injection fuel grain	Case 2	17.92	7.45	1

2.3.2. Grid Independence and Model Validation Analysis

A non-structured tetrahedral grid was employed to model both engine configurations. To ensure grid convergence, three mesh types were used to simulate both case 1 and case 2. The coarse, medium and fine meshes used in association with case 1 contained 0.93, 1.72 and 3.63 million cells, respectively, while those for case 2 comprised 1.55, 2.76 and 4.89 million cells, respectively. The average temperature and pressure along the axial cross-section located in the middle of each fuel grain were calculated and the results are summarized in Table 2. The differences between the results obtained using medium and fine meshes were negligible, indicating that convergence was obtained in both cases. Based on balancing computational time and accuracy, a medium mesh was selected for the subsequent numerical simulations.

Table 2. Results obtained from the grid independence study.

	Mesh Set	*T*, K	Relative Error, %	*P*, MPa	Relative Error, %
Case 1	Coarse	1869.01	5.25	2.20	2.8
	Medium	1770.88	0.28	2.11	1.4
	Fine	1775.85	0	2.14	0
Case 2	Coarse	2352.55	0.03	2.28	0.88
	Medium	2351.27	0.02	2.27	0.44
	Fine	2351.78	0	2.26	0

3. Results and Discussion

A series of firing tests was performed using the swirl-radial-injection fuel grains to investigate the combustion characteristics. The average oxidizer mass flow rates, $\dot{m}_{ox}$, average combustion pressures, P_c, and actual engine working times, t, during these trials are summarized in Table 3.

Table 3. Summary of test data.

No.	Fuel Grain	$\dot{m}_{ox}$, g/s	P_c, MPa	t, s
1	swirl-radial-injection fuel grain	7.45	0.51	3.98
2		11.22	0.88	4.16
3		14.28	1.73	4.79
4		15.87	1.88	4.19
5		17.92	1.47	4.06
6		20.73	1.68	3.7
7		20.87	2.04	3.85
8		25.67	2.06	3.89
9		24.57	2.63	4.04
10		27.57	3.00	3.8
11		30.68	2.69	3.74
12		30.25	2.54	3.81
13	paraffin-based fuel grain	10.53	0.78	4.31
14		18.45	1.42	4.18
15		24.86	2.01	4.09

3.1. Pressure and Image Analysis

The combustion chamber pressures and flame images obtained from the two different types of fuel grains at oxidizer flow rates of 11.9 and 19.05 g/s are compared in Figures 5 and 6, respectively. The oxidizer mass flow rates as functions of time (short dotted lines) are also presented in Figures 5 and 6. From Figure 5, it is evident that, after the engine ignited at t = 0 s, the combustion chamber pressure increased sharply then eventually reached a steady state. The maximum pressure obtained from the swirl-radial-injection fuel grain was slightly higher than that of the paraffin-based fuel grain during this plateau stage. Figure 6 shows similar data although, in this case, both fuel grains generated approximately the same steady state pressure. Both figures demonstrate that the paraffin-based fuel grain ignited slightly earlier than the swirl-radial-injection fuel grain.

Photographic images of exhaust plumes and of flames in the combustion chamber are also provided in Figures 5 and 6. It is worth noting that these images exhibit more significant changes than variations in the chamber pressure. Two points in time, corresponding to the ignition stage (t = 0.18 s for Figure 5 and t = 0.29 s for Figure 6) and the steady state (t = 3.45 s for Figure 5 and t = 3.44 s for Figure 6) were selected for analysis. As shown in Figure 5, during the initial ignition of the engine, both fuel grains generated a bright plume at the nozzle outlet. The chamber flame image gained from the paraffin-based fuel grain shows that the flame filled the entire field of view during this stage, meaning that the flame occupied the area from the pre-chamber to the main chamber. In contrast, in the case of the swirl-radial-injection fuel grain, the flame was concentrated inside the port. At t = 3.45 s, the exhaust plume of the paraffin-based fuel appears brighter than at 0.18 s. In addition, the combustion chamber flame image indicates that the flame continued to fill the entire field of view and was brighter than during the ignition stage. Interestingly, the swirl-radial-injection fuel grain produced a very smoky plume, suggesting that combustion occurred under fuel-rich conditions. As a consequence of this smoke, the camera lens was obscured and images of the combustion chamber could not be obtained. This obscuration of the lens by smoke was found to be ineradicable. This phenomenon may have been caused by a lack of flame in the pre-chamber, as was the case during ignition.

Data and images from trials using an oxidizer mass flow rate of 19.05 g/s are shown in Figure 6, from which it is evident that both grain types exhibited similar phenomena. Here, both grain types exhibit a bright plume during the ignition stage. The chamber flame images show that the paraffin-based fuel grain generated a flame that filled the entire field of view, while the swirl-radial-injection fuel grain produced a flame only in the port of the fuel grain. The former grain also showed a bright plume during the steady-state stage while that of the latter grain was smoky. Once more, the chamber flame associated with the paraffin-based fuel grain filled the entire field of view while images of the swirl-radial-injection fuel grain could not be acquired. Although the high-speed camera was unable to focus properly during the combustion of the paraffin-based fuel grains, possibly because of vibrations of the engine, this lack of focus did not affect our ability to assess the flame distribution.

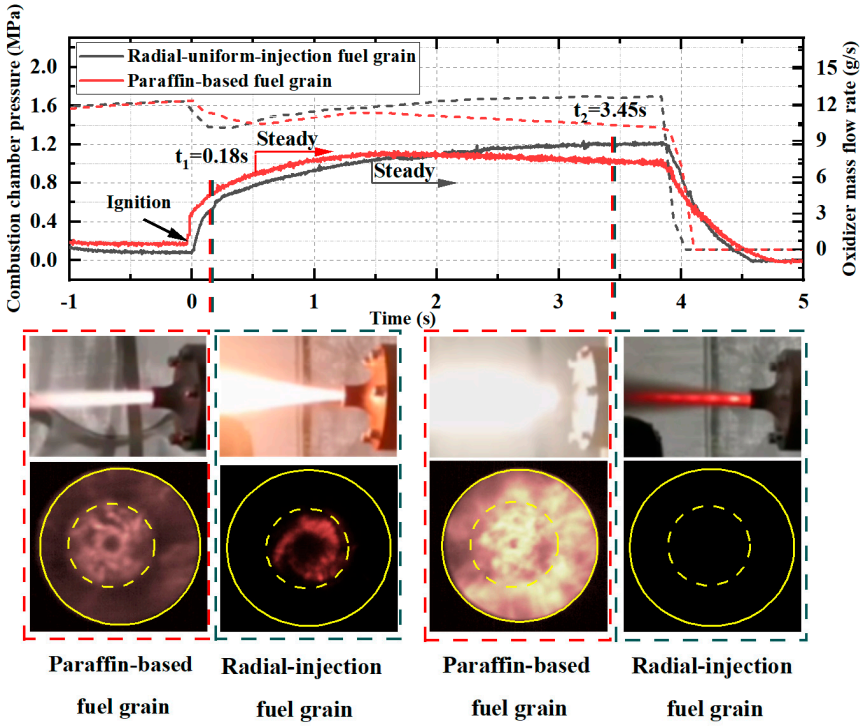

Figure 5. Plots of combustion chamber pressure and oxidizer mass flow rate over time and photographic images of the exhaust plumes and the flame in the combustion chamber at different times for two grain types, using an oxidizer flow rate of 11.90 g/s.

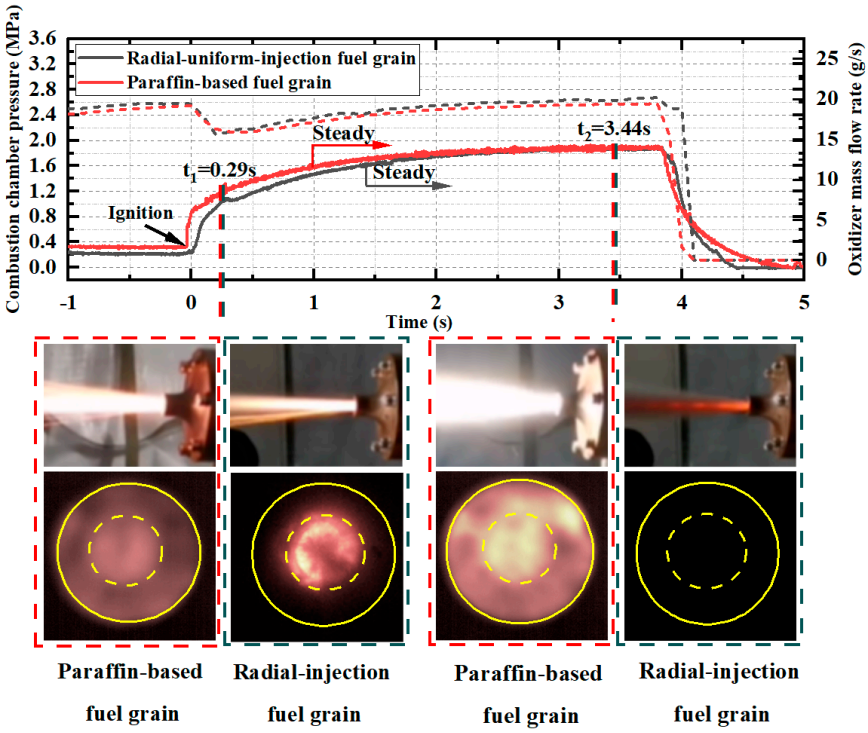

Figure 6. Plots of combustion chamber pressure and oxidizer mass flow rate over time and photographic images of the exhaust plumes and the flames in the combustion chambers at different times for the two grain types, using an oxidizer flow rate of 19.05 g/s.

3.2. Internal Morphologies of Fuel Grains

As shown in Figure 7, swirl-radial-injection fuel grains before and after the firing tests were cut along the axial center line and specimens were removed. The port diameters were subsequently measured at positions that were 0, 30, 60 and 90 mm from the front end, referred to herein as D1, D2, D3 and D4, respectively. The port diameter distributions along the axial directions of fuel grains following several tests are summarized in Figure 8. It is apparent from these data that there was no erosion at the front end of the fuel grain, in agreement with the images presented in Section 3.1, showing that the flame was only present in the port. This effect helped to provide thermal protection to the pre-chamber. It is also apparent from this figure that there were only slight variations in diameter along the axis direction. It should also be noted that the port diameter at the rear of the grain was slightly larger, in contrast to the results typically obtained from fuel grains using conventional fore-end injection. In such cases, the port diameter at the rear of the fuel grain is typically less than that at the front end [25,34,35].

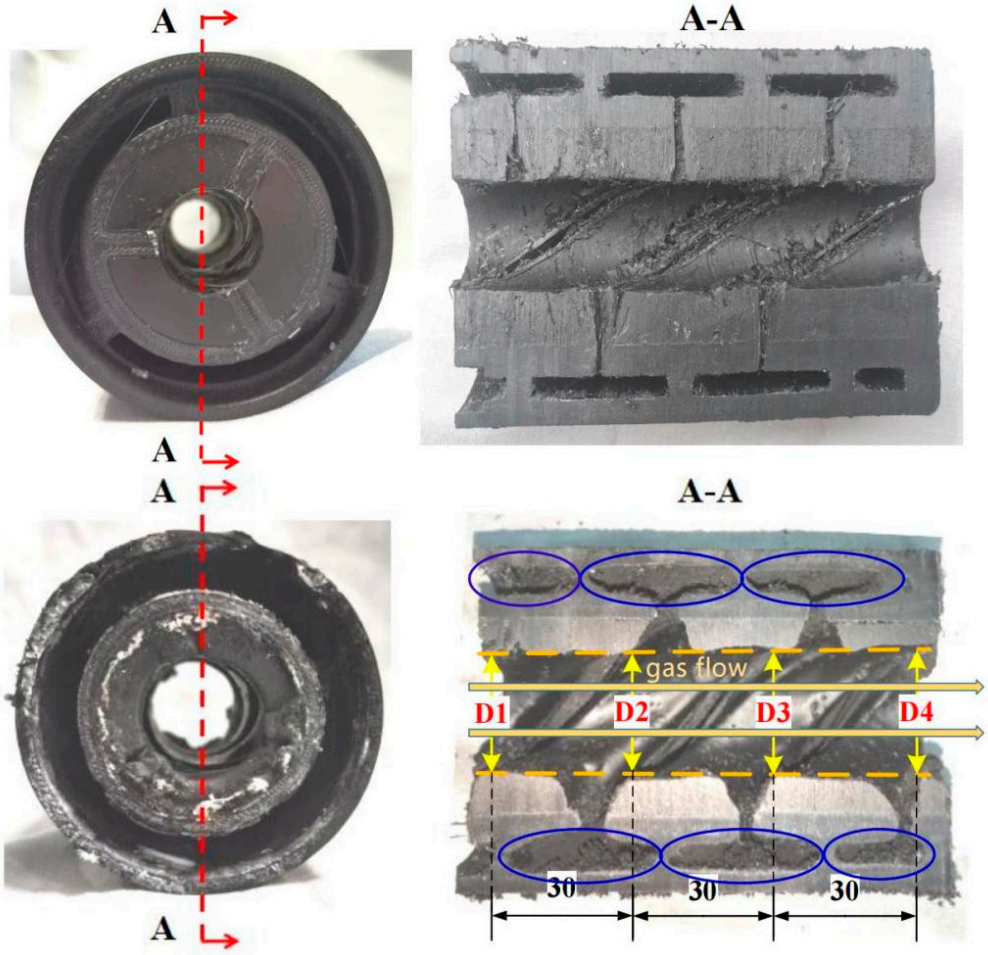

Figure 7. Fuel grain specimens excised from engines before and after firing tests (Yellow arrows mean the direction of gas flow and blue circles represent the areas of the oxidizer flow channel).

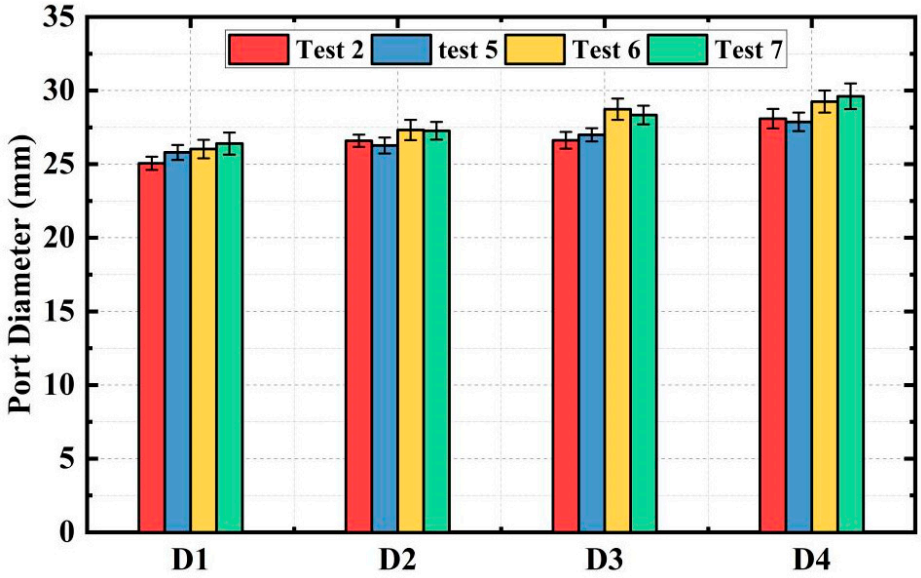

Figure 8. The port diameters of fuel grains at different axial positions after firing tests.

Erosion was also observed along the oxidizer flow channel at the outer wall, as indicated by the regions in the blue circles in Figure 5. This effect may have been caused by a low oxidizer flow velocity that allowed the flame to migrate into the oxidizer channels along the blades, as a consequence of the countercurrent flame propagation mechanism in this grain [36–39]. This phenomenon was expected to complicate subsequent evaluation of the fuel regression rate.

3.3. Regression Rates

Considering the oxidizer channel ablation phenomenon that occurred during the combustion of the present swirl-radial-injection fuel grains (see Section 3.2), calculating the regression rate solely based on the mass consumed during firing would have led to a large error. Hence, in this work, two alternative approaches to determining the regression rate were evaluated. In Method 1, only the mass lost based on the combustion of the paraffin-based fuel and the three blades was used in the calculation of equivalent port diameter while, in Method 2, the entire fuel grain mass loss was considered. These methods are explained in Figure 9b,c. The regions shaded in red in Figure 9 indicate the paraffin-based fuel was consumed while the blue shaded areas represent the ABS that was consumed. Two approaches were also used to ascertain the oxidizer mass flux values. In Method 1, the port diameter was measured at different axial positions after firing and these values were then averaged, while in Method 2, the equivalent port diameter was calculated based on the mass loss of the paraffin-based fuel and three blades. These calculations are described in detail in Appendix A. The regression rate results calculated using each of these methods had two sets of corresponding oxidizer mass flux results. Thus, four combinations of regression rate and oxidizer flux values were obtained and are summarized in Table 4. Four fitting lines to these data are plotted in Figure 10, in which the actual regression rates are distributed in the shaded regions. Here, the results of the paraffin-based fuel grains with fore-end injection are included as a baseline while a fitting line representing data obtained from the SP-1a fuel grain developed by Stanford University [40] is used as a reference. The present results demonstrate that, compared with the paraffin-based fuel grain, the regression rates of the swirl-radial-injection fuel grains were much improved.

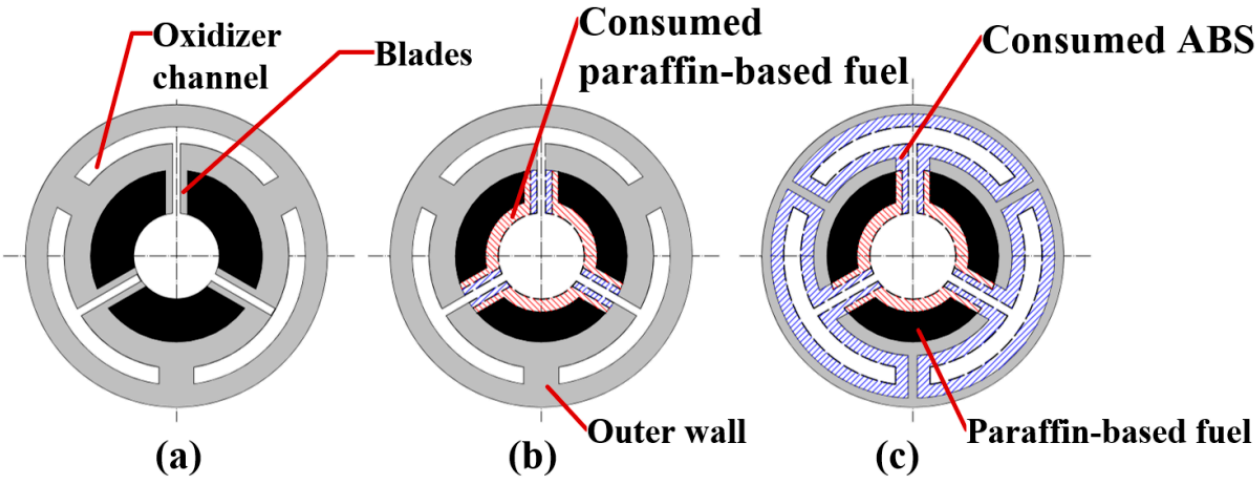

Figure 9. Diagrams showing fuel grain cross-sections (**a**) before a firing test, (**b**) after combustion of the entire fuel grain (as indicated by shading), and (**c**) after combustion of the paraffin-based fuel and the three blades (as indicated by shading).

Table 4. Methods used to determine regression rate and oxidizer flux.

Combination	1	2	3	4
Calculation method of oxidizer mass flux	1	2	1	2
Calculation method of regression rate	2	2	1	1
Fitting equation	$\dot{r} = 1.25G_{ox}^{0.44}$	$\dot{r} = 1.33G_{ox}^{0.44}$	$\dot{r} = 0.76G_{ox}^{0.41}$	$\dot{r} = 0.82G_{ox}^{0.40}$

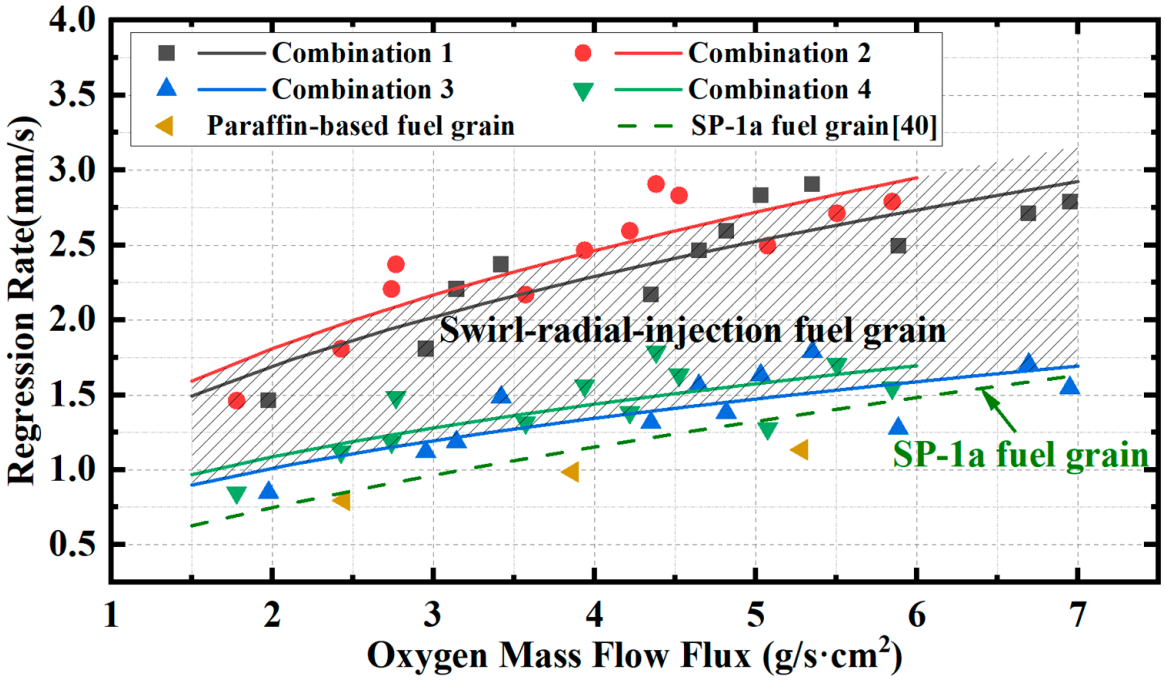

Figure 10. Comparison of the regression rates of swirl-radial-injection fuel grains with those of paraffin-based fuel grains and the SP-1a fuel grain.

3.4. Numerical Simulations

3.4.1. Analysis of Chemical Reactions

Figure 11 presents the temperature contours at cross-sections along the main view direction and in different axial directions for two cases. In case 1, which corresponded to the

fuel grain using fore-end injection, the oxygen entered the combustion chamber at the front end of the engine and reacted with the fuel to generate a typical HRE diffusion flame above the inner surface of the grain [41]. The simulated temperature in the pre-chamber was found to be relatively high, with a value of approximately 3700 K. Moving along the axis of the grain, oxygen was gradually consumed such that the flame slowly became thicker and moved away from the inner surface of the grain. Some residual oxygen evidently remained in the post-chamber and the flame was only present around the oxidizer flow.

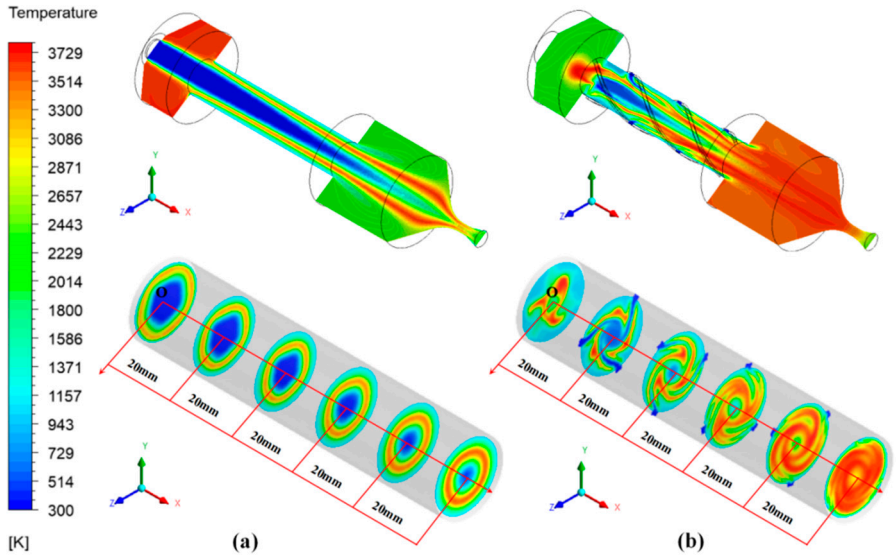

Figure 11. Temperature contours for cases (**a**) 1 and (**b**) 2.

The temperature contour for case 2 was very different from that of case 1. Here, the oxidizer was uniformly injected into the main chamber along the axial direction, which was more conducive to promoting mixing with the fuel. A helical flame appeared at the fuel grain port and the pre-chamber temperature was approximately 2000 K, which was much lower than that for case 1. These results were consistent with the lack of front-end erosion of the fuel grain as discussed in Section 3.2. With the axial position increasing, the flame zone became significantly bigger and closer to the inner surface of the fuel grain. The oxidizer was fully consumed in the post-chamber and the flame almost completely filled the post-chamber region.

The mass fractions of O_2, H_2O and CO_2 at the nozzle outlet for both cases are provided in Table 5. The engine using swirl-radial-injection fuel grain had a lower O_2 mass fraction at the outlet than that using paraffin-based fuel grain, indicating that more oxygen was reacted in the engine. In addition, the H_2O and CO_2 mass fractions at the outlet of this engine were higher. These data confirmed that more complete combustion would be expected to occur in this swirl-radial-injection fuel grain, based on using the mass fractions of CO_2 and H_2O as indicators of the extent of combustion [42].

Table 5. Mass fractions of various compounds at the nozzle outlet for the two engine configurations.

Species	Case 1	Case 2
O_2	0.159	0.033
H_2O	0.156	0.236
CO_2	0.194	0.244

The degree to which the combustion went to completion was quantified as a means of evaluating the efficiency of each design. The combustion efficiency, η_c, at a given location, x, can be defined based on the rate of H_2O generation or the rate of C_2H_4 consumption, written as [43]

$$\eta_c^{H_2O} = \frac{\dot{m}_{H_2O,x}}{\frac{\dot{m}_{C_2H_4,in}}{MW_{C_2H_4}} \times 4 \times \frac{1}{2} \times MW_{H_2O}} \times 100\% = \frac{\left[\int Y_{H_2O} \rho u dA\right]_x}{\frac{\dot{m}_{C_2H_4,in}}{MW_{C_2H_4}} \times 4 \times \frac{1}{2} \times MW_{H_2O}} \times 100\%, \quad (1)$$

and

$$\eta_c^{C_2H_4} = \frac{\dot{m}_{C_2H_4,in} - \dot{m}_{C_2H_4,x}}{\dot{m}_{C_2H_4,in}} \times 100\% = \frac{\dot{m}_{C_2H_4,in} - \left[\int Y_{C_2H_4} \rho u dA\right]_x}{\dot{m}_{C_2H_4,in}} \times 100\%, \quad (2)$$

where $\dot{m}_{H_2O,x}$, $\dot{m}_{H_2O,in}$ and $\dot{m}_{C_2H_4,x}$, $\dot{m}_{C_2H_4,in}$ are the H_2O or C_2H_4 mass flow rates through the channel at the inlet or at point x, respectively; ρ is the mixed gases density; $Y_{C_2H_4}$ is the mass fraction of C_2H_4; u is the axial velocity; and A is the cross-sectional area at point x.

The combustion efficiency values for 10 cross-sections ranging from the rear end of the fuel grain to the nozzle outlet were calculated, as shown in Figure 12. The data in the upper and lower plots in this figure were obtained using Equations (1) and (2), respectively. Here, the four dotted lines correspond to the rear of the fuel grain, the rear of the post-chamber section and the nozzle throat and outlet. The combustion efficiency as defined by Equation (1) for case 1 increased from 19.18% to 42.61%, going from the base of the fuel grain to the nozzle outlet, whereas for case 2, these values went from 45.41% to 59.07%. The combustion efficiency at the outlet of the nozzle was increased by 39.83% while the combustion efficiency at the rear of the fuel grain was 45.01% of the value at the outlet for case 1. For case 2, this value was 76.87%. These data are ascribed to the more complete combustion achieved at the base of the fuel grain with the new design. The combustion efficiency values defined by Equation (2) also exhibited the same trend. The combustion efficiencies at the rear of the fuel grain were determined to be 73.42% and 96.67%, respectively, for cases 1 and 2. Although the final combustion efficiency reached 100%, this occurred at approximately x = 40 and 10 mm for cases 1 and 2, respectively.

3.4.2. Analysis of Flow Field Characteristics

A 3D streamline diagram and several streamlines at different axial position cross-sections for case 1 and 2 are presented in Figure 13. It is obvious that rotational flow occurred at the center of the fuel grain in response to a viscous shear force and induction by the helical blades [44]. This flow promoted fuel/oxidizer mixing and so improved the combustion efficiency. The swirl flowing path also enhanced the shear action of the gas on the burning surface of the fuel grain, which in turn improved the regression rate.

The kinetic energy of turbulence reflects the intensity of the turbulence [44]. As shown in Figure 14, the kinetic energy values were minimal at the pre-chamber and the front end of the fuel grain. However, at axial positions close to the nozzle, the combustion reaction was significantly increased and so the turbulence kinetic energy was greater. Even so, the kinetic energy in the swirl-radial-injection engine was higher than that in the fore-end injection engine, indicating enhanced turbulence intensity in the former.

Although these numerical simulations were approximate, the results confirmed the potential to provide increased performance of the swirl-radial-injection fuel grain design. The extent of fuel/oxidizer mixing, the regression rate and the combustion efficiency were all greatly improved. Future work will focus on incorporating the solid fuel pyrolysis mechanism into these simulations and further optimizing the engine structure so as to reduce countercurrent flame propagation. Fuel grains containing different numbers of blades will also be assessed.

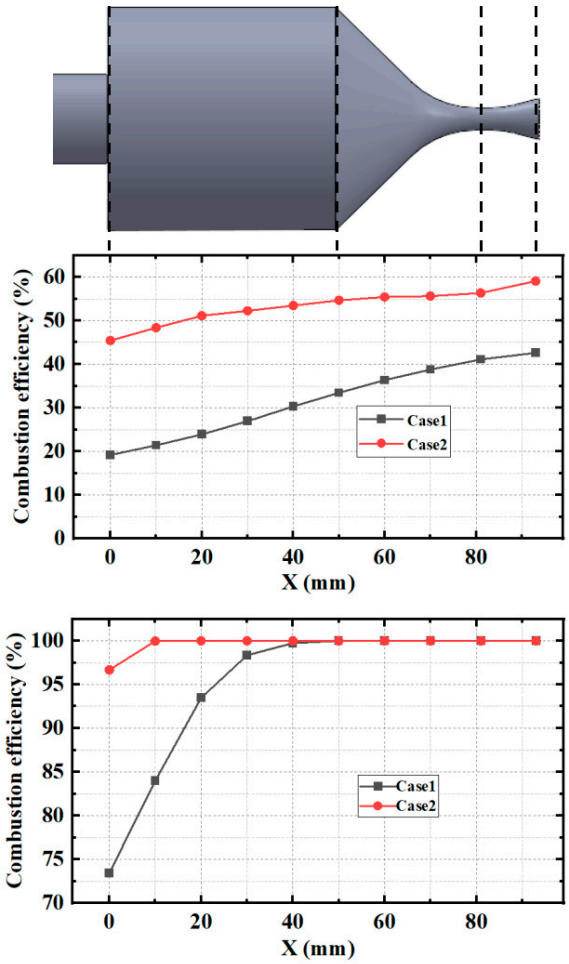

Figure 12. Combustion efficiency values for the two cases at various point along the grain as determined using Equation (1) (**upper**) and Equation (2) (**lower**).

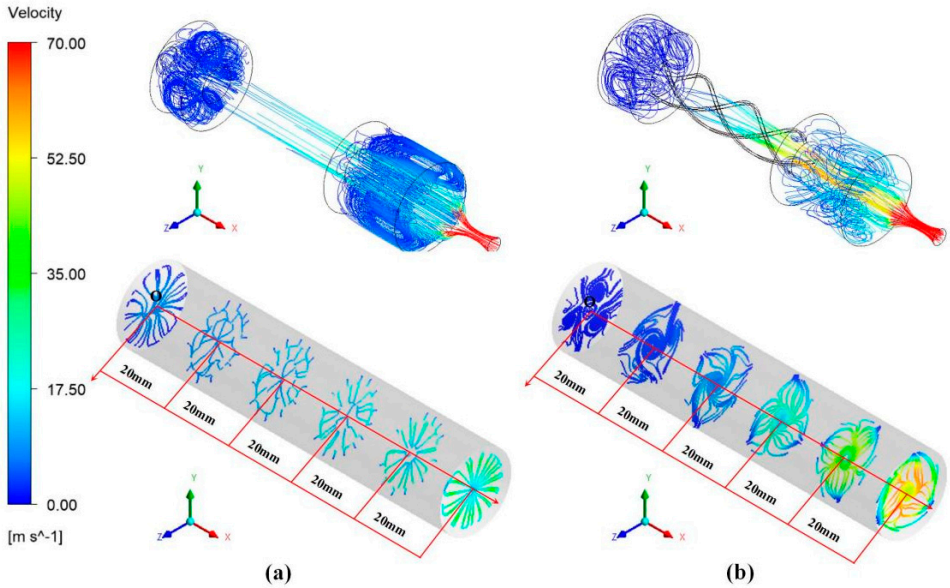

Figure 13. A 3D streamline and surface streamlines at different axial position cross-sections along the fuel grain for cases (**a**) 1 and (**b**) 2.

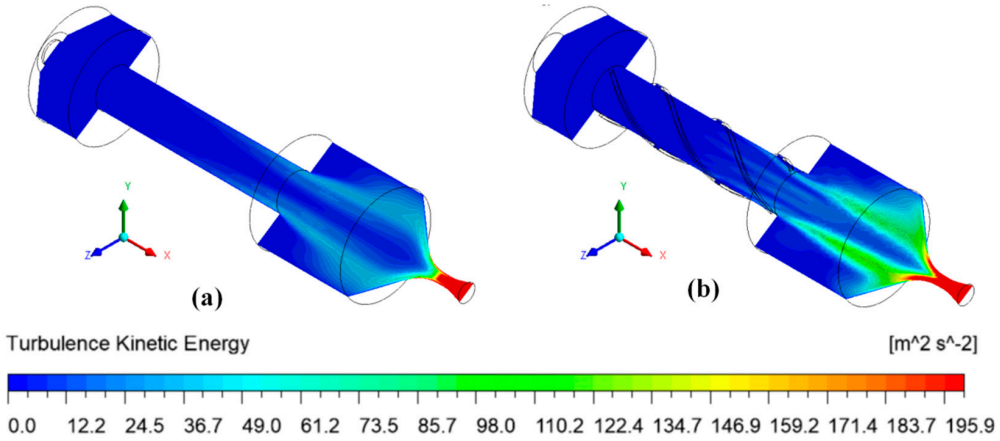

Figure 14. Distributions of turbulence kinetic energy along the main view cross-section for cases (**a**) 1 and (**b**) 2.

4. Conclusions

A swirl-radial-injection composite fuel grain consisting of an ABS substrate and paraffin-based fuel was designed and constructed. A series of experiments using laboratory scale HREs was conducted with oxidizer mass flux values in the range of 1.5 to 7 g/(s·cm^2) to explore combustion characteristics, including combustion chamber pressure, exhaust plume, port diameter distributions after firing and regression rates. Paraffin-based fuel grains using traditional fore-end injection were tested for comparison. The combustion efficiency, flame distribution and mechanism of regression rate enhancement were all investigated based on combustion simulations. The following conclusions can be made:

(1) Compared with the paraffin-based fuel grain using fore-end injection, the regression rate of the swirl-radial-injection fuel grain was considerably enhanced.

(2) Combustion chamber flame images could be acquired during the ignition stage. The images that were obtained showed that the flame was mainly concentrated in the port of the swirl-radial-injection fuel grain. This phenomenon mitigated front end ablation and reduced the difficulties associated with applying thermal protection to the pre-chamber.

(3) The combustion simulation results showed that the temperature in the pre-chamber of the swirl-radial-injection engine was significantly lower than that in the fore-end engine. Additionally, the fuel/oxidizer mixing effect was enhanced in the swirl-radial-injection fuel grain such that the combustion efficiency was greatly improved.

Author Contributions: Conceptualization, X.L.; Methodology, Z.W. and Z.Z.; Software, K.W.; Validation, X.L.; Formal analysis, R.W.; Resources, X.L.; Data curation, R.W. and Z.W.; Writing—original draft, R.W.; Writing—review & editing, X.L.; Visualization, J.L.; Supervision, X.L., Z.W., K.W., Z.Z., J.L., F.L. and X.Y.; Funding acquisition, X.L. All authors have read and agreed to the published version of the manuscript.

Funding: This work was funded in part by the National Natural Science Foundation of China (No. 92271117, No. 12072355 and No. 11872368, No. 11927803), Key-Area Research and Development Program of Guangdong Province, Grant No. 2021B0909060004, and the Youth Innovation Promotion Association of CAS (Grant No. 2022018).

Data Availability Statement: Data is unavailable due to privacy.

Conflicts of Interest: The authors declare no conflict of interest.

Appendix A Calculation of Regression Rate

As discussed in Section 3.3, two calculation methods were used to determine the regression rate and a further two methods employed to ascertain the oxidizer flux. These four calculation procedures are described in detail in this appendix.

Oxidizer flux calculation methods

The formula for calculating the oxidizer flux was

$$G_{ox} = \frac{\dot{m}_{ox}}{A}. \tag{A1}$$

The average port area of the fuel grain, A, can be determined as

$$A = \frac{A_0 + A_f}{2}, \tag{A2}$$

where A_0 and A_f are the average port area before and after the firing test, respectively. From these equations, it is evident that only the port area following the test will affect the oxidizer flux because the oxidizer mass flow rate and the initial port area are both fixed. On this basis, two methods were used to determine the port area.

Method 1 was based on measuring the inner diameters of the fuel grain at different axial locations and averaging these values. As discussed in Section 3.2, the port diameter was measured at locations that were 0, 30, 60 and 90 mm from the fore end with vernier calipers and the resulting values were used to calculate the average port area after each experiment. This method provided a larger oxidizer flux than the true value because the blades and oxidizer channel were also involved in the combustion.

Method 2 involved calculating the port area according to the mass of only the paraffin-based fuel and three blades that was consumed. The equivalent port diameter after tests, d_f, can be expressed as

$$d_f = \sqrt{d_0^2 + \frac{4\Delta m}{\rho L \pi}}, \tag{A3}$$

where d_0 is 20 mm in this work, Δm is the fuel mass consumed during the test, L is 100 mm and ρ is the average density of the solid fuel involved in combustion.

The paraffin-based fuel and ABS substrate were separated after the test and weighed to determine the mass of paraffin-based fuel consumed during the tests. As shown in Figure A1a, removing the transparent part allowed access to the region used to calculate the port area (indicated in Figure A1b). It is evident that the mass difference should also include the mass of the blades because these parts were fully involved in the combustion process. The volume of the blades was determined using the Quality Properties parameter in the SolidWorks software program and multiplied by the ABS density of 0.92 g/cm^3 to obtain the mass of the blades.

The ρ was calculated as

$$\rho = \rho_p \omega_p + \rho_{ABS} \omega_{ABS}, \tag{A4}$$

where ρ and ω are density and mass fraction, respectively, and subscripts p and ABS represent values corresponding to the paraffin-based fuel and ABS, respectively. The regression rate was calculated as

$$\dot{r} = \frac{\sqrt{d_0^2 + \frac{4\Delta m}{\rho L \pi}} - d_0}{2t}, \tag{A5}$$

where d_0, Δm, ρ and L are the same as those in Equation (A3) and t is the working time of the HRE.

Method 1 employed the mass of the three blades and paraffin-based fuel consumed during the test. In this method, the Δm values were determined in the same manner as

was employed in Method 2 to calculate the oxidizer flux, meaning that only the mass of the paraffin-based fuel and blades that was consumed was considered. The fuel mass consumed in the oxidizer channel was not taken into account.

Method 2 used the mass of the entire fuel grain consumed during firing. In this case, the fuel grain was weighed before and after the experiment to give Δm and the regression rate was obtained by substituting all quantities into Equation (A5). However, ablation in the oxidizer channel resulting from the countercurrent flame propagation caused the results calculated by this method to be larger than the actual value. In summary, four combinations of regression rate and oxidizer flux values were obtained. Following this, four fitting formulas were calculated based on the formula

$$\dot{r} = aG_{ox}^{n}. \tag{A6}$$

The fitting formulas are presented in Section 3.3.

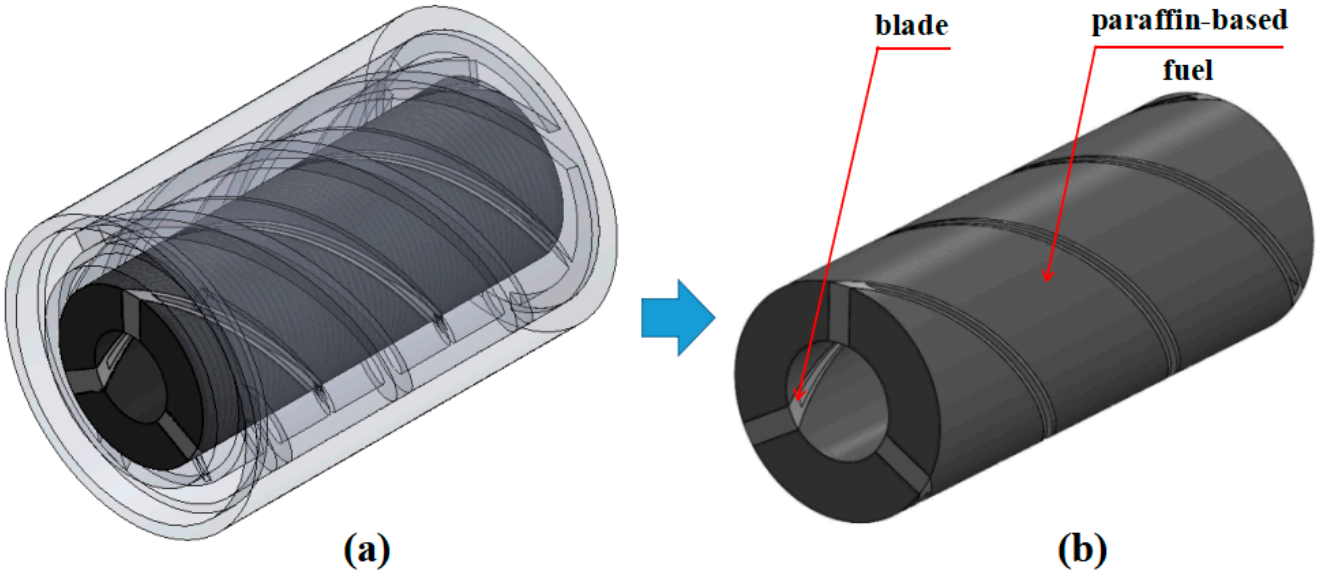

Figure A1. Diagrams showing (**a**) the entire fuel grain and (**b**) the region used to calculate the port area.

References

1. Mazzetti, A.; Merotto, L.; Pinarello, G. Paraffin-based hybrid rocket engines applications: A review and a market perspective. *Acta Astronaut.* **2016**, *126*, 286–297. [CrossRef]
2. Okninski, A.; Kopacz, W.; Kaniewski, D.; Sobczak, K. Hybrid rocket propulsion technology for space transportation revisited-Propellant solutions and challenges. *FirePhysChem* **2021**, *1*, 260–271. [CrossRef]
3. Durand, J.; Lestrade, J.-Y.; Anthoine, J. Restitution methodology for space and time dependent solid-fuel port diameter evolution in hybrid rocket engines. *Aerosp. Sci. Technol.* **2021**, *110*, 106497. [CrossRef]
4. Glaser, C.; Gelain, R.; Bertoldi, A.; Levard, Q.; Hijlkema, J.; Lestrade, J.-Y.; Hendrick, P.; Anthoine, J. Experimental regression rate profiles of stepped fuel grains in Hybrid Rocket Engines. *Acta Astronaut.* **2023**, *204*, 186–198. [CrossRef]
5. Wei, S.-S.; Lee, M.-C.; Huang, J.-W.; Lu, Y.; Kang, C.-H.; Kao, S.-T.; Lu, S.-J.; Huang, C.-H.; Zhan, J.-J.; Chen, Z.-R.; et al. Demonstration of tethered hovering flight of HTTP-3AT hybrid rocket. *Acta Astronaut.* **2022**, *191*, 279–292. [CrossRef]
6. Wang, Y.; Hu, S.-Q.; Liu, X.-L.; Liu, L.-L. Boundary layer combustion of HTPB/paraffin fuels for hybrid propulsion applications. *Aerosp. Sci. Technol.* **2022**, *129*, 107850. [CrossRef]
7. Karabeyoglu, M.; Cantwell, B.; Altman, D. Development and testing of paraffin-based hybrid rocket fuels. In Proceedings of the 37th Joint Propulsion Conference and Exhibit, Salt Lake City, UT, USA, 8–11 July 2001. [CrossRef]
8. Fabiani, M.; Gubernari, G.; Migliorino, M.T.; Bianchi, D.; Nasuti, F. Numerical Simulations of Fuel Shape Change and Swirling Flows in Paraffin/Oxygen Hybrid Rocket Engines. *Aerotec. Missili Spaz.* **2022**, *102*, 91–102. [CrossRef]
9. Tian, H.; Wang, Z.; Zhu, H.; Lu, Y.; Gao, J.; Cai, G. Effect of High-Mass Fraction of Aluminum on Catalytic Hybrid Rocket Motor. *Appl. Sci.* **2022**, *12*, 13023. [CrossRef]
10. Marxman, G.; Gilbert, M. Turbulent boundary layer combustion in the hybrid rocket. In *Symposium (International) on Combustion*; Elsevier BV: Amsterdam, The Netherlands, 1963; Volume 9, pp. 371–383. [CrossRef]

11. Sezaki, C.; Sakamoto, M.; Hirata, K.; Yuasa, S.; Sakurai, T.; Shiraishi, N. Measurement of Axial-Direction Fuel Regression Rate of Swirling-Oxidizer-Flow-Type Hybrid Rocket Engines. In Proceedings of the 46th AIAA/ASME/SAE/ASEE Joint Propulsion Conference & Exhibit, Nashville, TN, USA, 25–28 July 2010. [CrossRef]
12. Granado, E.Q.; Hijlkema, J.; Lestrade, J.-Y.; Anthoine, J. Pseudo-Two-Dimensional Modeling and Validation of a Hybrid Rocket Combustion Chamber. *J. Propuls. Power* **2022**, *38*, 957–972. [CrossRef]
13. Whitmore, S.A.; Walker, S.D. Engineering Model for Hybrid Fuel Regression Rate Amplification Using Helical Ports. *J. Propuls. Power* **2017**, *33*, 398–407. [CrossRef]
14. Lee, J.; Moon, H.; Kim, J. Thermal-Combustion Coupled Instability in Hybrid Rockets with Fuel Blowing. *J. Propuls. Power* **2023**, *39*, 308–317. [CrossRef]
15. Di Martino, G.D.; Carmicino, C.; Savino, R. Transient Computational Thermofluid-Dynamic Simulation of Hybrid Rocket Internal Ballistics. *J. Propuls. Power* **2017**, *33*, 1395–1409. [CrossRef]
16. Berwal, P.; Biswas, S. Experimental Investigation on Combustion Characteristics of Hybrid Rocket Fuels with Multi-Angle Diverging Injector. *Int. J. Turbomach. Propuls. Power* **2020**, *5*, 12. [CrossRef]
17. Cai, G.; Li, C.; Tian, H. Numerical and experimental analysis of heat transfer in injector plate of hydrogen peroxide hybrid rocket motor. *Acta Astronaut.* **2016**, *128*, 286–294. [CrossRef]
18. Kumar, R.; Thamizarasan, K. Use of N_2O–O_2 as the Oxidizer for the Hybrid Rocket Application. In Proceedings of the National Aerospace Propulsion Conference: Select Proceedings of NAPC 2020, Bengaluru, India, 17–19 December 2020. [CrossRef]
19. Zdybal, D.; Pabarcius, L.; Laczewski, A.; Wyciszkiewicz, B.; Zwolak, A.; Slawecki, P.; Wyzlinski, M. Investigation of FDM-printed open-framework-reinforced helical PEWAX grains as a robust, high regression hybrid rocket fuel. In Proceedings of the AIAA Scitech 2021 Forum, Online, 11–15, 19–21 January 2021. [CrossRef]
20. Vignesh, B.; Kumar, R. Effect of multi-location swirl injection on the performance of hybrid rocket motor. *Acta Astronaut.* **2020**, *176*, 111–123. [CrossRef]
21. Yuasa, S.; Yamamoto, K.; Hachiya, H.; Kitagawa, K.; Oowada, Y. Development of a small sounding hybrid rocket with a swirling-oxidizer-type engine. In Proceedings of the 37th Joint Propulsion Conference and Exhibit, Salt Lake City, UT, USA, 8–11 July 2001. [CrossRef]
22. Bisin, R.; Paravan, C. A new strategy for the reinforcement of paraffin-based fuels based on cellular structures: The armored grain—Ballistic characterization. *Acta Astronaut.* **2023**, *206*, 284–298. [CrossRef]
23. Wang, Z.; Lin, X.; Li, F.; Yu, X. Combustion performance of a novel hybrid rocket fuel grain with a nested helical structure. *Aerosp. Sci. Technol.* **2020**, *97*, 105613. [CrossRef]
24. Lin, X.; Qu, D.; Chen, X.; Wang, Z.; Luo, J.; Meng, D.; Liu, G.; Zhang, K.; Li, F.; Yu, X. Three-dimensional printed metal-nested composite fuel grains with superior mechanical and combustion properties. *Virtual Phys. Prototyp.* **2022**, *17*, 437–450. [CrossRef]
25. Zhang, Z.; Lin, X.; Wang, Z.; Wu, K.; Luo, J.; Fang, S.; Zhang, C.; Li, F.; Yu, X. Effects of swirl injection on the combustion of a novel composite hybrid rocket fuel grain. *Acta Astronaut.* **2022**, *199*, 174–182. [CrossRef]
26. Saiga, S.; Shirahama, A.; Aso, S.; Tani, Y.; Shimada, T. A Study on O/F Shift of Aft Counter-Swirl Oxidizer Injection with Multi-Section Swirl Injection Method for Hybrid Rocket. In Proceedings of the AIAA Scitech 2019 Forum, San Diego, CA, USA, 7–11 January 2019. [CrossRef]
27. Ohe, K.; Oyama, S.; Araki, K.; Aso, S.; Tani, Y.; Shimada, T. Study on Hybrid Rocket with Multi-Section Swirl Injection Method toward Flight Experiments of Subscale Space Plane. In Proceedings of the 50th AIAA/ASME/SAE/ASEE Joint Propulsion Conference, Cleveland, OH, USA, 28–30 July 2014. [CrossRef]
28. Araki, K.; Hirata, Y.; Oyama, S.; Ohe, K.; Aso, S.; Tani, Y.; Shimada, T. A Study on Performance Improvement of Paraffin Fueled Hybrid Rocket Engines with Multi-Section Swirl Injection Method. In Proceedings of the 49th AIAA/ASME/SAE/ASEE Joint Propulsion Conference, San Jose, CA, USA, 14–17 July 2013. [CrossRef]
29. Kahraman, M.; Ozkol, I.; Karabeyoglu, A. Enhancement of Fuel Regression Rate for Hybrid Rockets by Introducing Novel Coaxial Tube Injector. In Proceedings of the AIAA Propulsion and Energy 2020 Forum, Online, 24–28 August 2020. [CrossRef]
30. Bisin, R.; Paravan, C.; Alberti, S.; Galfetti, L. A new strategy for the reinforcement of paraffin-based fuels based on cellular structures: The armored grain—Mechanical characterization. *Acta Astronaut.* **2020**, *176*, 494–509. [CrossRef]
31. Luo, J.; Zhang, Z.; Lin, X.; Wang, Z.; Kun, W.; Zhou, G.; Zhang, S.; Li, F.; Yu, X.; Wu, J. Flame Dynamics in the Combustion Chamber of Hybrid Rocket Using Multiangle Chemiluminescence. *J. Propuls. Power* **2023**, *39*, 482–491. [CrossRef]
32. Migliorino, M.T.; Gubernari, G.; Bianchi, D.; Nasuti, F.; Cardillo, D.; Battista, F. Numerical Simulations of Fuel Shape Change in Paraffin-Oxygen Hybrid Rocket Engines. *J. Propuls. Power* **2023**, 1–15. [CrossRef]
33. Løvås, T.; Malik, N.; Mauss, F. Global Reaction Mechanism for Ethylene Flames with Preferential Diffusion. *Combust. Sci. Technol.* **2010**, *182*, 1945–1960. [CrossRef]
34. Shinohara, K.; Nakagawa, I. Regression Rate Characteristics of Paraffin-based Fuel under Swirled Oxidizer Flow. In Proceedings of the 48th AIAA/ASME/SAE/ASEE Joint Propulsion Conference & Exhibit, Atlanta, Georgia, 30 July–1 August 2012. [CrossRef]
35. Saburo, Y.; Noriko, S.; Kousuke, H. Controlling Parameters for Fuel Regression Rate of Swirling-oxidizer-flow-type Hybrid Rocket Engine. In Proceedings of the 48th AIAA/ASME/SAE/ASEE Joint Propulsion Conference & Exhibit, Atlanta, Georgia, 30 July–1 August 2012. [CrossRef]
36. Zhou, S.; Gao, J.; Wu, J.; Zhang, D. Countercurrent flame propagation inside vertical PMMA cylinders against pure oxygen flow. *Combust. Flame* **2022**, *246*, 112396. [CrossRef]

37. Jia, S.; Hu, L.; Ma, Y.; Zhang, X.; Fujita, O. Experimental study of downward flame spread and extinction over inclined electrical wire under horizontal wind. *Combust. Flame* **2022**, *237*, 111820. [CrossRef]
38. Wu, Y.; Zhang, Z.; Wang, Q.; Wang, N. Combustion characteristics of skeleton polymer reinforced paraffin-wax fuel grain for applications in hybrid rocket motors. *Combust. Flame* **2022**, *241*, 112055. [CrossRef]
39. Carney, A.; Li, Y.; Liao, Y.-T.; Olson, S.; Ferkul, P. Concurrent-flow flame spread over thin discrete fuels in microgravity. *Combust. Flame* **2021**, *226*, 211–221. [CrossRef]
40. Karabeyoglu, A.; Zilliac, G.; Cantwell, B.J.; DeZilwa, S.; Castellucci, P. Scale-Up Tests of High Regression Rate Paraffin-Based Hybrid Rocket Fuels. *J. Propuls. Power* **2004**, *20*, 1037–1045. [CrossRef]
41. Zhang, S.; Hu, F.; Wang, D.; Okolo, N.P.; Zhang, W. Numerical simulations on unsteady operation processes of N_2O/HTPB hybrid rocket motor with/without diaphragm. *Acta Astronaut.* **2017**, *136*, 115–124. [CrossRef]
42. Islam, M.; Ahmed, Z.U.; Hossain, K.A. Numerical analysis of LOx-BioLPG combustion in high-pressure liquid rocket engine propulsion system. *South Afr. J. Chem. Eng.* **2023**, *45*, 83–99. [CrossRef]
43. Zhang, Z.; Wu, K.; Yuen, R.; Yao, W.; Wang, J. Numerical investigation on the performance of bluff body augmented micro cavity-combustor. *Int. J. Hydrogen Energy* **2020**, *45*, 4932–4945. [CrossRef]
44. Ju, J.; Duan, X.; Sarkodie, B.; Hu, Y.; Jiang, H.; Li, C. Numerical simulation of flow field and residence time of nanoparticles in a 1000-ton industrial multi-jet combustion reactor. *Chin. J. Chem. Eng.* **2021**, *51*, 86–99. [CrossRef]